RSC Advances

PAPER

View Article Online
View Journal | View Issue

Cite this: *RSC Adv.*, 2017, **7**, 10200

Terbium and holmium codoped yttrium phosphate as non-contact optical temperature sensors

Hongwei Fang,[a] Xiantao Wei,[a] Shaoshuai Zhou,[b] Xinyue Li,[c] Yonghu Chen,[a] Chang-Kui Duan*[a] and Min Yin*[a]

Optical thermometry has attracted many studies for non-contact high-resolution real-time temperature sensing. Most promising approaches are based on the ratio of up-converted luminescence intensities of two thermally coupled excited states. Here, we proposed a new strategy utilizing the temperature dependence of the anti-Stokes luminescence by exciting a thermally populated low-lying state to the excited state. Our scheme not only retains the advantage of previous approaches in reducing noise from the Stokes-type stray light, but also has the advantage of high quantum yield as a result of a one-photon excitation process. The temperature-dependent luminescence of Tb^{3+}, Ho^{3+} codoped YPO_4 is employed to demonstrate our scheme. The results show that, under a certain excitation, the emission of Tb^{3+} enhances dramatically while that of Ho^{3+} declines with increasing temperature. The sharp temperature-dependent intensity ratio was used to calibrate temperature. A maximum relative sensitivity of 2.51% K^{-1} at 310 K was obtained, substantially superior to values previously reported for acknowledged optical thermometry phosphors. These results indicate that the YPO_4:Tb^{3+},Ho^{3+} can be a promising candidate to achieve accurate optical temperature sensing with a high sensitivity, and the mechanism proposed can be used to develop better optical thermometry.

Received 9th December 2016
Accepted 1st February 2017

DOI: 10.1039/c6ra27971f

rsc.li/rsc-advances

1. Introduction

Non-contact optical temperature sensors have been attracting extensive attention because of their wide applications as molecular probes and nano-thermometry.[1–4] Some schemes based on spectral shift, emission bandwidth, absolute intensity, fluorescence lifetime, as well as fluorescence intensity ratio (FIR), have been widely explored.[5–9] Among these aspects, FIR of two thermally-coupled energy levels (TCELs) based on up-conversion (UC) luminescence is adopted frequently.[10–13] Compared to conventional down-conversion luminescence, UC luminescence can effectively reduce the interference of Stokes-type stray scattering light from sensors and their environment. However, the fluorescence quantum yield of UC luminescence tends to be very low (usually much less than 1% under weak excitation intensity), which means that, to obtain good signal to noise ratio, one has to drastically enhance the laser power, but this often causes heating of the sensor. Besides, the common FIR technique is based on the assumption of transient thermoequilibrium between the two TCELs, which may break down at low temperature when the nonradiative relaxation between the two TCELs is not fast enough, *i.e.*, loss of thermal coupling.

Under the premise of retaining the advantage of UC luminescence and aiming to effectively prompt the fluorescence quantum yield, we consider an alternative mechanism to achieve luminescence temperature sensing. In this work, as the temperature-detection region in our case ranges from room temperature to high temperature (above 700 K), the tetragonal phase yttrium phosphate YPO_4 with xenotime structure was chosen as the host material when given its good physical and chemical stability at high temperature.[14] Meanwhile, rare-earth ions with TCELs were widely investigated to achieve FIR sensing based on UC luminescence, such as Nd^{3+}, Gd^{3+}, Dy^{3+}, Ho^{3+}, Er^{3+} and Tm^{3+}.[15–21] Trivalent terbium have a $4f^7$ electronic configuration, and the energy gap between the ground state $^7F_6$ and the first excited state $^7F_5$ is roughly 2100 cm^{-1}, which suggests that the thermal equilibrium between $^7F_5$ and $^7F_6$ can be constructed at a relatively high temperature. In YPO_4, Tb^{3+} and Ho^{3+} were both expected to substitute for Y^{3+} in YPO_4. Under a certain pulsed laser excitation and by monitoring the characteristic emission of both Ho^{3+} and Tb^{3+}, we can obtain the FIR between these two emissions. By calculation, we found the sample YPO_4:Tb^{3+},Ho^{3+} has a high relative sensitivity, which shows the sample can be a potential candidate to achieve high-sensitivity temperature sensing.

[a]*Key Laboratory of Strongly-Coupled Quantum Matter Physics, Chinese Academy of Science, School of Physical Sciences, University of Science and Technology of China, No. 96 Jinzhai Road, Hefei, Anhui Province, 230026, P. R. China. E-mail: yinmin@ustc.edu.cn; ckduan@ustc.edu.cn*

[b]*Department of Physics, Qufu Normal University, Qufu, Shandong Province, 273165, P. R. China*

[c]*College of Materials & Environmental Engineering, Hangzhou Dianzi University, Hangzhou, Zhejiang Province, 310018, P. R. China*

2. Experimental

2.1. Materials synthesis

Tb^{3+}, Ho^{3+}-codoped YPO_4 powder sample was synthesized *via* hydrothermal method. Firstly, $RE(NO_3)_3$ standard solutions (RE = Y, Tb, Ho and Y/Tb/Ho = 96 : 3.2 : 0.8) were prepared by dissolving the respective Y_2O_3, Tb_4O_7 and Ho_2O_3 (99.99%) in hot dilute nitric acid with the total metal cations being 2 mmol. After vigorous magnetic stirring for 15 min, $NH_4H_2PO_4$ was added to the mixed solution. Then, the pH value of the mixture was adjusted to 1 with adding moderate amount of dilute nitric acid. Continuously stirring and several minutes later, the mixture were transferred to the muffle furnace at 160 °C for 18 h. The white precipitate was separated by centrifugation and washed with deionized water and ethanol for several times. And then the precipitate was dried at 60 °C for 2 h and the collected powder was calcined at 850 °C for 4 h in the air. Subsequently after ground, the powder was recalcined at 1200 °C for 8 h under CO reduction atmosphere.

2.2. Materials characterization

The as-prepared phosphors were characterized by an X-ray diffractometer (MAC Science Co., Ltd., MXP18AHF, Tokyo, Japan) using nickel-filtered Cu Kα radiation (λ = 0.15418 nm), with the accelerating voltage and tube current being 40.0 kV and 100.0 mA, respectively. The photoluminescence excitation (PLE) and emission (PL) spectra were measured by a double monochromator (Model Jobin-Yvon HRD-1) equipped with a Hamamatsu R928 photomultiplier. The excitation source was a tunable laser system (Opolette 355 LD system) which has a laser linewidth of 4–7 cm^{-1} and a pulse duration of 7 ns. The detected signal was analyzed by an EG&G 7265 DSP Lock-in Amplifier and the decay curves were recorded with a Tektronix TDS2024 digital storage oscilloscope (US Patents, Shanghai, China).

3. Results and discussion

3.1. Phase characterization

The crystal structure was identified by the XRD patterns in Fig. 1. As shown, all diffraction peaks of the sample fit well with the standard JCPD 74-2479, and no additional peaks are found, indicating no impurity was introduced in our samples.

3.2. Room-temperature luminescence properties

Fig. 2(a) shows the photoluminescence excitation (PLE) and emission (PL) spectra of Tb^{3+} singly-doped YPO_4. As presented, the PLE spectrum of YPO_4:Tb^{3+} consists of several excitation peaks located at 345.0, 355.0, 362.0, 370.0 and 381.0 nm, respectively. Under 370.0 nm excitation, the PL spectrum consists of several characteristic emission peaks which can be attributed to $^5D_{3,4}$–^7F_J transition of Tb^{3+}. The transitions we care about are $^5D_4$–$^7F_5$ (543.9 nm) and $^5D_4$–$^7F_6$ (488.0 nm). Fig. 2(b) shows the PLE and PL spectrum of Ho^{3+} singly-doped YPO_4. Under 362.0 nm excitation, some characteristic emission peaks centered at 641.0, 645.0 and 658.0 nm can be observed, which of all can be ascribed to the $^5F_5$–$^5I_8$ transition of Ho^{3+}.[22] We can observe from Fig. 2 that, Tb^{3+} and Ho^{3+} have similar characteristic peaks at around 540.0 nm, which provides the possibility to simultaneously excite Tb^{3+} and Ho^{3+} under a certain excitation wavelength.

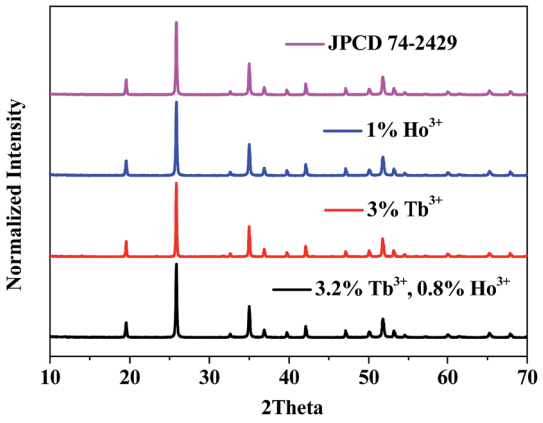

Fig. 1 XRD patterns of (a) YPO_4:4%Tb^{3+}, (b) YPO_4:1%Ho^{3+} and (c) YPO_4:3.2%Tb^{3+},0.8%Ho^{3+} powder samples. The standard JPCD card (no. 74-2429) is presented as a reference.

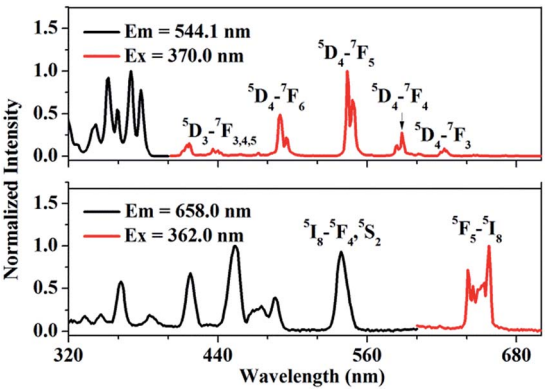

Fig. 2 Photoluminescence excitation (PLE) and emission spectra (PL) of (a) Tb^{3+}-singly doped YPO_4 and (b) Ho^{3+}-singly doped YPO_4 at room-temperature.

3.3. Temperature-dependent luminescence properties of YPO_4:Tb^{3+},Ho^{3+}

The schematic diagram of the mechanism for temperature sensing is depicted in Fig. 3. Tb^{3+} and Ho^{3+} can be simultaneously excited under a certain excitation, and the transitions we concern about are $^7F_5$–$^5D_4$ of Tb^{3+} and $^5I_8$–$^5F_4$ ($^5S_2$) of Ho^{3+}. The thermally-activated Tb^{3+} which locates at the lowest excited state stark level of $^7F_5$ multiplets can be excited to $^5D_4$ state *via* resonance absorption, followed by the radiative transitions from $^5D_4$ to ^7F_J states, and we detect the emission between $^5D_4$ to $^7F_6$. In theory, as the system is in thermal equilibrium, the population of Tb^{3+} situated at $^7F_5$ and $^7F_6$ follows the Boltzmann distribution. Therefore, as the temperature rises, the number of Tb^{3+} being excited to $^5D_4$ increases correspondingly and so does the emission intensity, which means that this emission can be

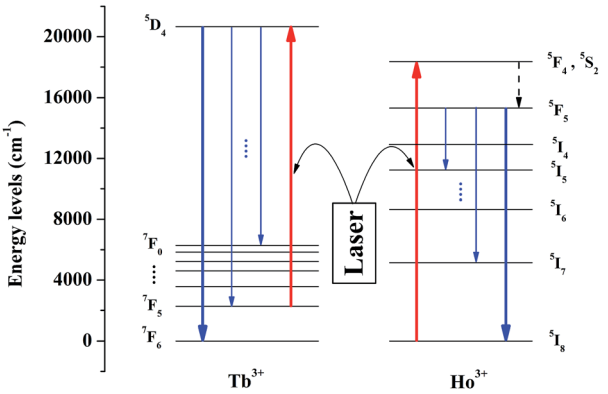

Fig. 3 Schematic energy level diagram of Tb^{3+} and Ho^{3+} in YPO_4. Under a certain excitation, the excitation we care about are $^7F_6$–$^5D_4$ (Tb^{3+}) and $^5I_8$–$^5F_4$, $^5S_2$ (Ho^{3+}), and the emission we concern are $^5D_4$–$^7F_6$ (Tb^{3+}) and $^5F_5$–$^5I_8$ (Ho^{3+}).

utilized to measure the temperature variation. Meanwhile, Ho^{3+} was doped as a reference to ensure the accuracy of the luminescence intensity of Tb^{3+}. Under the same excitation, Ho^{3+} situated in the ground state $^5I_8$ can be excited to $^5F_4$ ($^5S_2$) and due to the non-radiative relaxation from $^5F_4$ ($^4S_2$) to $^5F_5$, the emission of $^5F_5$–$^5I_8$ transition can be observed.

According to this inspiration, we investigated the temperature-dependent emission of $^5D_4$–$^7F_6$ transition of Tb^{3+}, as well as $^5F_5$–$^5I_8$ transition of Ho^{3+} in our as-prepared YPO_4:-Tb^{3+},Ho^{3+} powder sample under excitation of 543.9 nm, which suits well to the resonance absorption of Tb^{3+} at room temperature. In order to ensure strong emission intensity of Tb^{3+} and effectively reduce the energy transfer between Tb^{3+} and Ho^{3+}, we choose 3.2% and 0.8% as the doping concentration of Tb^{3+} and Ho^{3+}, respectively. The emission spectra were measured at various temperatures between 310 K and 760 K, ranging from 470.0 to 510.0 nm and from 630.0 to 670.0 nm which corresponds to the transition of $^5D_4$–$^7F_6$ of Tb^{3+} and $^5F_5$–$^5I_8$ of Ho^{3+}, respectively. As shown in Fig. 4, under 543.9 nm excitation, the absolute luminescence intensity of Tb^{3+} enhances monotonously with increasing temperature until 730 K and nearly keeps invariant when the temperature further rises to 760 K.

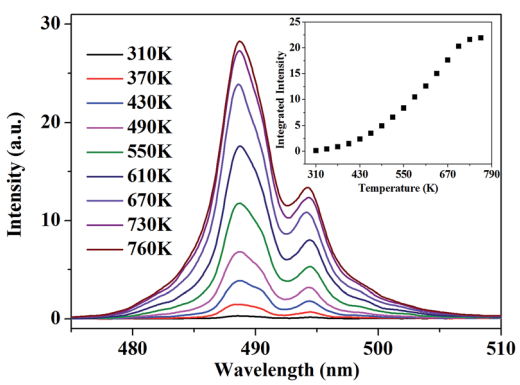

Fig. 4 PL spectra of $^5D_4$–$^7F_6$ transition under 543.9 nm excitation at various temperature. The inset shows the variation of the integrated fluorescence intensity with temperature.

To quantitatively present the temperature-dependent variation, we obtained the integrated fluorescence intensity ranging from 470.0 nm to 510.0 nm of $^5D_4$–$^7F_6$ transition of Tb^{3+}. The experimental data are fitted with the Arrhenius formula:[1]

$$I(T) \sim \exp\left(\frac{-\Delta E}{k_B T}\right), \quad (1)$$

where k_B is Boltzmann constant. An effective energy difference $\Delta E = 1846$ cm^{-1} is obtained. This value is smaller than the energy gap between $^7F_5$ and $^7F_6$ of Tb^{3+}, which is estimated to be 2100 cm^{-1} from the emission spectrum. Fig. 5 presents the logarithmic integrated fluorescence intensity in response to the inverse of temperature. An obvious deviation from the calculated energy gap can be explicitly observed. This is due to the fact that apart from the variation of population of $^7F_5$ of Tb^{3+}, some other factors such as variations with temperature of absorption efficiency and luminescent quantum efficiency need to be taken into account.

The obvious deviation is mainly linked to the variation of excitation efficiency at various temperature. Fig. 6 shows the PLE spectra at various temperature. The inset presents that the peak position of PLE spectrum witnesses a slight red-shift (about 2 Å) as temperature increases. Due to the sharp spectral shape in PLE spectra, the proportion of 543.9 nm in the whole excitation range can be largely influenced by the shift of temperature-dependent excitation peaks, leading to the declining excitation efficiency contributing to the $^5D_4$–$^7F_6$ emission of Tb^{3+}.

In addition, the decay curves depending on temperature is given in Fig. 7. The fluorescence lifetime of $^5D_4$ of Tb^{3+} can be determined from the decay curves by monitoring the emission of $^5D_4$–$^7F_5$ at 543.9 nm under the excitation of $^7F_6$–$^5D_4$ at 488.0 nm. Fig. 7 shows the normalized decay curves at a series of temperatures, which presents that the lifetime of $^5D_4$ nearly keeps invariant over the whole temperature range concerned, indicating there is little thermal quenching of Tb^{3+} and weak energy transfer between Tb^{3+} and Ho^{3+}. The decay curve can be well fitted by double exponential equation:

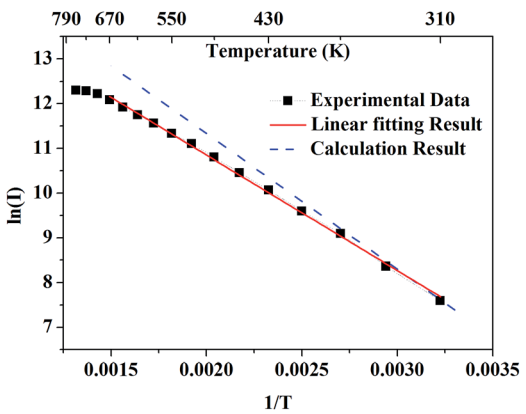

Fig. 5 The black solid rectangles present the logarithmic integrated fluorescence intensity in response to the inverse of temperature. The red solid line presents the linear fitting result of experimental data. The blue dashed line presents the theoretical results calculated from the emission spectrum.

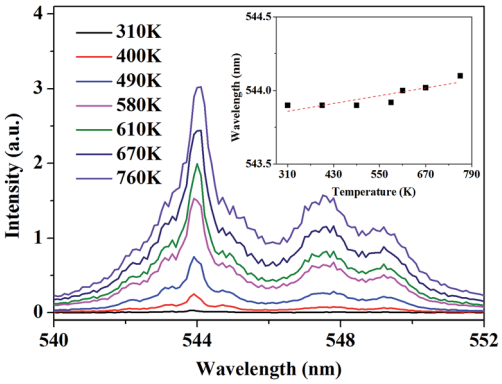

Fig. 6 The PLE spectra monitored at 488.0 nm at various temperature. The Inset shows the shift of peak position with increasing temperature.

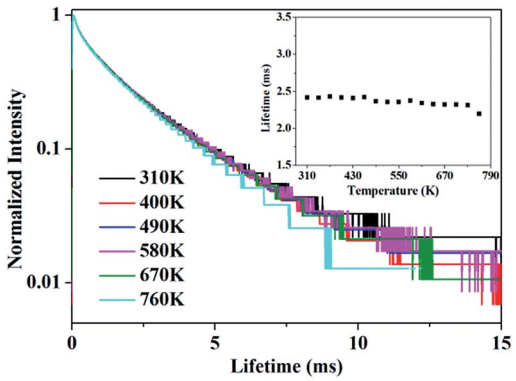

Fig. 7 The decay curve of $^5D_4$ energy level of Tb^{3+} when monitored at 543.9 nm under 488.0 nm excitation. The inset shows the variation of luminescence lifetime of $^5D_4$ with various temperature.

$$I(t) = A\exp(-t/\tau_1) + B\exp(-t/\tau_2), \quad (2)$$

where I is the luminescence intensity, A and B are constants, t is the time, τ_1 and τ_2 are the decay time for the two exponential components, respectively. The result shows that the fluorescence decay curve consists of fast and slow decay components, which may due to the different doping concentration distribution in our sample.[23] The average lifetime can be calculated by the following formula:

$$\tau = \frac{\int I(t)t\mathrm{d}t}{\int I(t)\mathrm{d}t} = \frac{A\tau_1^2 + B\tau_2^2}{A\tau_1 + B\tau_2}. \quad (3)$$

The calculated average lifetime is obtained to be ~2.40 ms at the temperature of 310–760 K.

It can be concluded from Fig. 6 that, more dramatic variation of the emission of Tb^{3+} which contributes to larger FIR value will be obtained if we adjust the excitation wavelength from 543.9 nm to 544.1 nm. Under 544.1 nm excitation, the emission spectra ranging from 470.0 to 510.0 nm and 630 to 670 nm were measured at various temperatures ranging from 310 K to 760 K corresponding to $^5D_4$–$^7F_6$ transition of Tb^{3+} and $^5F_5$–$^5I_8$ transition of Ho^{3+}, respectively. From Fig. 8, it can be explicitly observed that the luminescence intensity of Tb^{3+} witnesses a monotonous increase while the tendency of Ho^{3+} gradually decrease with rising temperature. As temperature increases, the enhancing luminescence intensity of Tb^{3+} is mainly linked with the larger population in $^7F_5$, while the declining intensity of Ho^{3+} is appropriately accounted by the common multiple-photon relaxation process between $^5F_5$ and $^5I_4$ when given the large phonon energy of YPO_4 (about 1080 cm^{-1}) and small energy difference between $^5F_5$ and $^5I_4$ (less than 2400 cm^{-1}).[24]

To effectively reduce the effect of noise and avoid the overlap of emission between Tb^{3+} and Ho^{3+}, we choose the integrated area of a certain range within 486.0–496.0 nm of Tb^{3+} and 657.0–661.0 nm of Ho^{3+} rather than a whole range. The integrated fluorescence intensity from these two ranges were calculated to quantitatively depict the temperature-dependent variation, and the FIR between Tb^{3+} and Ho^{3+} depending on temperature is presented in Fig. 9. To better understand the temperature sensing performance, it is of great significance to investigate the sensing sensitivity for an optical thermometer. The relative sensitivity S_R is a key parameter to evaluate the

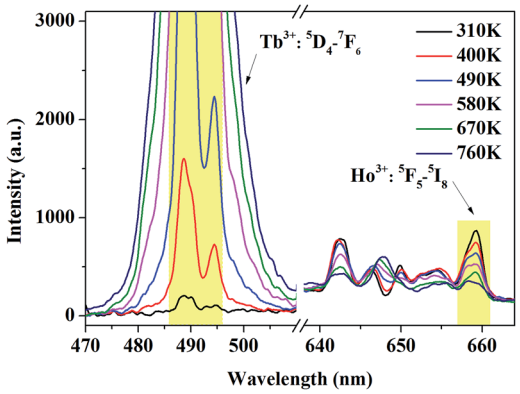

Fig. 8 Temperature-dependent absolute intensity of $^5D_4$–$^7F_6$ transition of Tb^{3+} and $^5F_5$–$^5I_8$ transition of Ho^{3+} under 544.1 nm excitation. The integrated range to obtain FIR is selected as 486.0–496.0 nm for Tb^{3+} and 657.0–661.0 nm for Ho^{3+}.

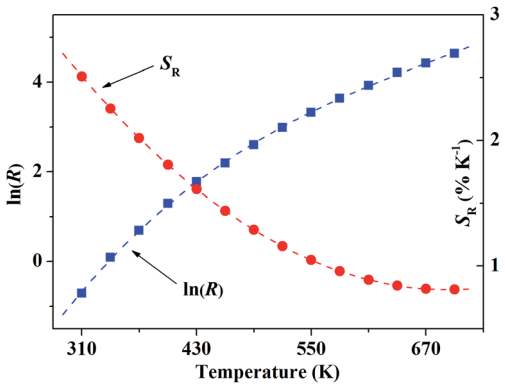

Fig. 9 The blue solid rectangles present ln(*R*) in response to the temperature. The red dashed line is the polynomial fitting curve, which just describe the variation tendency of the data.

Table 1 Compared with other previously reported rare-earth ions doped temperature sensors, the sensitivity of our sample is much higher, especially at room temperature.[15–20,25,26] The result indicates that YPO_4:Tb^{3+}, Ho^{3+} can be a potentially excellent candidate for optical temperature sensors with high relative sensitivity

Materials	The range of T (K)	$S_{R\ max}$ (% K^{-1})	S_R at 300 K (% K^{-1})
PKBAN glass:Nd^{3+} (ref. 15)	300–450	1.50	1.50
NaLuF4:Yb^{3+},Tm^{3+},Gd^{3+} (ref. 16)	300–460	1.26	0.74
$Y_4Al_2O_9$:Dy^{3+} (ref. 17)	300–420	1.60	1.60
Y_2O_3:Yb^{3+},Ho^{3+} (ref. 18)	299–419	1.19	1.19
$AgLa(MoO_4)_2$:Yb^{3+},Er^{3+} (ref. 19)	298–458	1.26	1.26
$NaYF_4$:Yb^{3+},Tm^{3+},Pr^{3+} (ref. 20)	300–460	1.53	0.42
$LiAl_5O_3$:Cr^{3+} (ref. 25)	300–480	0.83	0.21
$NaGd(MoO_4)_2$:Tb^{3+},Pr^{3+} (ref. 26)	303–483	2.05	0.61
YPO_4:Tb^{3+},Ho^{3+}	310–550	2.60	2.60

property of the sensors, which is defined as the relative change of the FIR (denoted as R) in response to the variation of temperature, which can be obtained by the following equation:

$$S_R = \frac{1}{R}\frac{dR}{dT}. \quad (4)$$

Fig. 9 shows the relationship of $\ln(R)$ and S_R in response to the temperature T. As many factors have to be considered in our case, the variation of FIR cannot be quantitatively described by a simple model, so the data was dealt with polynomial fitting just to present the variation tendency of $\ln(R)$ in response to T.

According to formula (4), the corresponding relative sensitivity for our sample is given within the temperature range of 310–700 K, which is displayed in Fig. 8 as well. The result of polynomial fitting shows the S_R can be described approximately with

$$S_R = 0.06378 - (16.07 \times 10^{-5})T + (11.60 \times 10^{-8})T^2 \quad (5)$$

The calculated S_R value reaches around 2.60% K^{-1} at $T = 300$ K. Several typical temperature sensors based on FIR technique and their relative sensitivity were displayed in Table 1. Compared with other previously reported rare-earth ions doped temperature sensors, the sensitivity of our sample is much higher, especially at room temperature.[15–20,25,26] The result indicates that YPO_4:Tb^{3+},Ho^{3+} can be a potentially excellent candidate for optical temperature sensors with high relative sensitivity.

4. Conclusion

We proposed a scheme for optical temperature sensing and implemented it with the material YPO_4:3.2%Tb^{3+},0.8%Ho^{3+}. In our sample, the relative sensitivity S_R can reach the value of 2.60% at 300 K, which is superior to many other common temperature sensing materials, which indicates that YPO_4:Tb^{3+},Ho^{3+} can be a potential candidate as optical temperature sensor. The sample YPO_4:Tb^{3+},Ho^{3+} based on the FIR between $^5D_4$–$^7F_6$ of Tb^{3+} and $^5F_5$–$^5I_8$ of Ho^{3+} serves as a way of temperature sensing not only bearing the advantages of both UC luminescence and FIR techniques but also dramatically enhancing the fluorescence quantum yield, which presents excellent temperature-dependent luminescence properties with a high sensing sensitivity. Furthermore, as the scheme is mainly based on the energy structure of Tb^{3+} and Ho^{3+} in our case, host materials and doping ions can be further explored to optimize the luminescence properties and sensing sensitivity.

Acknowledgements

The authors are thankful for the financial support of National Natural Science Foundation of China (Grants no. 11374291, 11204292, 11274299, 11574298, 11404320 and 11604037) and the National Key Research and Development Program of China (2016YFB0701001).

Notes and references

1 X. D. Wang, O. S. Wolfbeis and R. J. Meier, *Chem. Soc. Rev.*, 2013, **42**, 7834–7869.
2 S. L. Shinde and K. K. Nanda, *Angew. Chem., Int. Ed.*, 2013, **52**, 11325–11328.
3 S. H. Zheng, W. B. Chen, D. Z. Tan, J. J. Zhou, Q. B. Guo, W. Jiang, C. Xu, X. F. Liu and J. R. Qiu, *Nanoscale*, 2014, **6**, 5675–5679.
4 X. J. Xue, F. Wang and X. G. Liu, *J. Mater. Chem.*, 2011, **21**, 13107–13127.
5 O. A. Savchuk, G. P. Haro, J. J. Carvajal, D. Jaque, J. Massons, O. M. Aguil and F. Díaz, *Nanoscale*, 2014, **6**, 9727–9733.
6 E. H. Song, S. Ding, M. Wu, S. Ye, F. Xiao, G. P. Dong and Q. Y. Zhang, *J. Mater. Chem. C*, 2013, **1**, 4209–4215.
7 S. S. Zhou, X. Y. Li, X. T. Wei, C. K. Duan and M. Yin, *Sens. Actuators, B*, 2016, **231**, 641–645.
8 M. K. Mahata, K. Kumar and V. K. Rai, *Sens. Actuators, B*, 2015, **209**, 775–780.
9 D. Q. Chen, Z. Y. Wan, Y. Zhou, X. Z. Zhou, Y. L. Yu, J. S. Zhong, M. Y. Ding and Z. G. Ji, *ACS Appl. Mater. Interfaces*, 2015, **7**, 19484–19493.
10 S. A. Wade, S. F. Collins and G. W. Baxter, *J. Appl. Phys.*, 2003, **94**, 4743–4756.
11 O. A. Savchuk, J. J. Carvajal, C. Cascales, M. Aguilo and F. Díaz, *ACS Appl. Mater. Interfaces*, 2016, **8**, 7266–7273.

12 K. Z. Zheng, Z. Y. Liu, C. J. Lv and W. P. Qin, *J. Mater. Chem. C*, 2013, **1**, 5502–5507.
13 A. Pandey, V. K. Rai, V. Kumar and H. C. Swart, *Sens. Actuators, B*, 2015, **209**, 352–358.
14 Z. L. Xiu, Z. S. Yang, M. K. Lu, S. W. Liu, H. P. Zhang and G. J. Zhou, *Opt. Mater.*, 2006, **29**, 431–434.
15 P. Rodríguez, L. L. Martín, S. F. L. Luis, I. R. Martín, K. K. Kumar and C. K. Jayasankar, *Sens. Actuators, B*, 2014, **195**, 324–331.
16 K. Zheng, Z. Liu, C. Lv and W. Qin, *J. Mater. Chem. C*, 2013, **1**, 5502–5507.
17 Z. Boruc, M. Kaczkan, B. Fetlinski, S. Turczynski and M. Malinowski, *Opt. Lett.*, 2012, **37**, 5214–5216.
18 A. Pandey and V. K. Rai, *Dalton Trans.*, 2013, **42**, 11005–11011.
19 T. Li, C. F. Guo, S. S. Zhou, C. K. Duan and M. Yin, *J. Am. Ceram. Soc.*, 2015, 1–5.
20 S. Zhou, G. Jiang, X. Li, S. Jiang, X. Wei, Y. Chen, M. Yin and C. Duan, *Opt. Lett.*, 2014, **39**, 6687–6690.
21 J. Cao, X. Li, Z. Wang, Y. Wei, L. Chen and H. Guo, *Sens. Actuators, B*, 2016, **224**, 507–513.
22 R. Capelletti, A. Baraldi, E. Buffagni, M. Mazzera, N. Magnani, E. M. Rodriguez, J. G. Solé and M. Bettinelli, *Spectrosc. Lett.*, 2010, **43**, 382–388.
23 J. Y. Sun, X. Y. Zhang, Z. G. Xia and H. Y. Du, *J. Appl. Phys.*, 2012, **111**, 013101.
24 O. K. Moune, M. D. Faucher and N. Edelstein, *J. Lumin.*, 2002, **96**, 51–68.
25 X. Y. Li, G. C. Jiang, S. S. Zhou, X. T. Wei, Y. H. Chen and C. K. Duan, *Sens. Actuators, B*, 2014, **202**, 1065–1069.
26 Y. Gao, F. Huang, L. Hang, J. Zhou, J. Xu and Y. S. Wang, *Adv. Funct. Mater.*, 2016, **26**, 3139–3145.